Color-gradient lattice Boltzmann modeling of immiscible two-phase flows on partially wetting surface

Yuan Yu[1,3,4], Haihu Liu[2], Yonghao Zhang[3] and Dong Liang[1,4]

[1]School of Engineering, Sun Yat-sen University, Guangzhou, China

[2]School of Energy and Power Engineering, Xi'an Jiaotong University, Xi'an, China

[3]Department of Mechanical and Aerospace Engineering, University of Strathclyde, Glasgow, United Kingdom

[4]Guangdong Provincial Key Laboratory of Fire Science and Technology, Guangzhou, China

Abstract

A zero-interfacial-force condition is derived and implemented to improve the wetting boundary scheme for a lattice Boltzmann color-gradient model. This new wetting boundary scheme is validated by two static problems, i.e. a droplet resting on a flat surface and a cylindrical surface, and one dynamic problem, i.e. the capillary filling in a 2 dimensional (2D) channel. In these simulations, we observe that non-physical mass transfer is suppressed and spurious velocities become smaller. Meanwhile, accurate results including dynamic contact line movement are achieved on a broad range of contact angles. The model is then applied to study displacement of immiscible fluids in a 2D channel. Both the displacement velocity and the change rate of finger length are found to exhibit a linear dependence on the contact angle at the viscosity ratio of unity. The displacement velocity decreases but the change rate of finger length increases with increasing capillary number, while the displacement velocity tends to be constant, i.e. two-third of the maximum inlet velocity, at high viscosity ratios or low capillary numbers. In contrast to the displacement velocity, the change rate of finger length is negligible at high viscosity ratios or low capillary numbers, where the finger length is in an equilibrium state, while the equilibrium finger length itself is smaller at a higher viscosity ratio or a lower capillary number.

Keywords

Color-gradient lattice Boltzmann model, wetting boundary scheme, interfacial force, immiscible displacement, contact line movement

Introduction

Multiphase flows are ubiquitous in nature and industrial processes. In recent decades, the lattice Boltzmann (LB) models have been developed to simulate the multiphase flows. These models mostly fall into one of the following categories[1, 2]: the color-gradient model[3, 4], the pseudopotential model[5-8], the

[a] Author to whom correspondence should be addressed. Electronic mail (a): haihu.liu@mail.xjtu.edu.cn; (b): gzliangd@163.com

[b] Peer-reviewed accepted author manuscript of the following in press output: Yu, Y., Liu, H., Zhang, Y., & Liang, D. (2017). Color-gradient lattice Boltzmann modeling of immiscible two-phase flows on partially wetting surface. Proceedings of the Institution of Mechanical Engineers, Part C: Journal of Mechanical Engineering Science .

free-energy model[9-14] and the mean-field theory model[15]. The fluid-structure interaction[16-21] and wettability treatment[4, 6, 22-24] based on the LB community are the key research hotspots. Numerical studies of these interfacial dynamics usually use diffuse interface models[25-28] or sharp interface models[29, 30]. It is known that the diffuse interface models[26, 28] have advantages in describing near-critical interfacial phenomena, dynamic contact line, contact angle hysteresis, breakup or coalescence of droplets or bubbles. In a diffuse interface model, there are usually two ways to impose the appropriate wetting condition, i.e. the surface-energy formulation[27, 31, 32] based on Young's equation of constant surface tension and the so-called geometric formulation for a prescribed contact angle θ_s[26].

The surface-energy formulation scheme differs from the geometric formulation for a prescribed contact angle[26, 33], where the non-physical mass transfer (NPMT) effect, which is defined as a fictive mass transfer beyond the theoretical phase interface, is very obvious especially when the contact angle is less than 90 degrees[6, 24]. Physically, the precursor film is an effect beyond the hydrodynamic scale, so no spreading beyond the nominal contact line region should be observed in the surface-energy formulation. The root cause of evident NPMT effect in surface-energy formulation scheme is the conflict between two assumptions. In the surface-energy formulation, fluid property $\varphi_s(\boldsymbol{x})$, e.g. density, is imposed on the virtual fluid nodes, the surface tension between fluid and solid can then be expressed. Substituting the surface tension into the Young's equation, we obtain a relationship between the fluid property $\varphi_s(\boldsymbol{x})$ and contact angle θ. Noting that the Young's equation assumes a sharp interface and works only in contact line region. If we impose the virtual fluid property $\varphi_s(\boldsymbol{x})$ on all the solid surface nodes in a diffuse interface model, these two assumptions, i.e. sharp interface and diffuse interface, conflict each other.

The geometric formulation can avoid this conflict and eliminate the NPMT effect for the surface-energy formulation even in the single-phase region. For example, in the first geometric formulation model, Ding et al.[26] chose the tangential component $|\boldsymbol{\tau}\cdot\boldsymbol{\nabla}\rho^N|$ as the reference, which is used to introduce the prescribed contact angle by only adjusting the normal component $\boldsymbol{n}\cdot\boldsymbol{\nabla}\rho^N = -|\boldsymbol{\tau}\cdot\boldsymbol{\nabla}\rho^N|\cot\theta$ at each time step. As a result, the NPMT effect no longer appears in single-phase region, but the reference $|\boldsymbol{\tau}\cdot\boldsymbol{\nabla}\rho^N|$ is under the severe restriction of the isotropic order of DnQb lattice stencil especially in a contact line region. When the contact angle is very small or very large, the reference $|\boldsymbol{\tau}\cdot\boldsymbol{\nabla}\rho^N|$ and isotropic truncation error have the same order of magnitude, which leads to failure of accuracy. Improving the isotropic order or adopting eccentric isotropic difference can mitigate this problem. To impose this geometric formulation for curved boundaries, Leclaire et al.[24] used the modulus $|\boldsymbol{\nabla}\rho^N|$ as the reference instead of the tangential component $|\boldsymbol{\tau}\cdot\boldsymbol{\nabla}\rho^N|$, the reference $|\boldsymbol{\nabla}\rho^N|$ is now always large enough for the isotropic truncation error even in small or large contact angle cases.

However, there are still some issues to be resolved. Firstly, an effective way for a dynamic problem to estimate the unit normal vector $\boldsymbol{n}_f$ of $\boldsymbol{\nabla}\rho^N$ on the outermost fluid nodes is needed. The linear least squares method is adopted in Leclaire's method[24], which works well for static contact angle problems, but it fails for dynamic problems because the vector $\boldsymbol{n}_f$ changes dramatically in the contact line region, the linear or bilinear interpolation cannot be used to fit the spatial function of vector $\boldsymbol{n}_f$. Secondly, the NPMT effect in the contact line region is needed to be minimized, which profoundly affects the stability and accuracy.

Here, a new wetting boundary scheme is proposed based on the LB color-gradient model of Liu et al.[4], which can effectively control the NPMT effect in both the single-phase and contact line regions, and manifest accurate contact line movement. A zero-interfacial-force condition is derived based on the diffuse interface assumption in contact line region, which is essential for calculation of the interface curvature. This wetting boundary scheme is first validated by two static problems, i.e. a droplet resting

on a flat surface and a cylindrical surface, and one dynamical problem, i.e. the capillary filling in a 2D channel. The displacement of immiscible fluids in a 2D channel is then studied, and the effects of the surface wettability, capillary number and the viscosity ratio on the displacement process are systematically examined.

Numerical method

Lattice Boltzmann multiple-relaxation-time color-gradient model

A color-gradient LB model[34, 35], which was developed from the works of Lishchuk et al.[36] and Halliday et al.[37, 38], is adopted in this study. The color-gradient model consists of three steps, i.e. the collision step, the recoloring step and the streaming step. Two distribution functions $f_{\alpha,R}$ and $f_{\alpha,B}$ are introduced to represent two immiscible fluids, i.e. red fluid and blue fluid, and the subscript α denotes the αth direction of the lattice velocity. The total distribution function is defined by $f_\alpha = f_{\alpha,R} + f_{\alpha,B}$, which undergoes a collision step as

$$f'_\alpha(\boldsymbol{x}, t) = f_\alpha(\boldsymbol{x}, t) + \Omega_\alpha(\boldsymbol{x}, t) + \bar{F}_\alpha(\boldsymbol{x}, t) \tag{1}$$

where $\boldsymbol{x}$ and t are the position and time respectively, f'_α is the post-collision distribution function, Ω_α is the collision operator, and $\bar{F}_\alpha$ is the forcing term. In the multiple-relaxation-time (MRT) framework, the collision operator is given by

$$\Omega_\alpha(\boldsymbol{x}, t) = -(\boldsymbol{M}^{-1}\boldsymbol{S}\boldsymbol{M})_{\alpha\beta}\left[f_\beta(\boldsymbol{x}, t) - f_\beta^{eq}(\boldsymbol{x}, t)\right] \tag{2}$$

where f_β^{eq} is the equilibrium distribution functions of f_β, $\boldsymbol{M}$ is a transformation matrix and $\boldsymbol{S}$ is a diagonal relaxation matrix. The equilibrium distribution function is defined in a polynomial form with respect to the local velocity $\boldsymbol{u}$, which is obtained from the Maxwell-Boltzmann distribution:

$$f_\alpha^{eq}(\rho, \boldsymbol{u}) = \rho w_\alpha\left[1 + \frac{\boldsymbol{e}_\alpha \cdot \boldsymbol{u}}{c_s^2} + \frac{(\boldsymbol{e}_\alpha \cdot \boldsymbol{u})^2}{2c_s^4} - \frac{\boldsymbol{u}^2}{2c_s^2}\right] \tag{3}$$

where $\rho = \rho_R + \rho_B$ is the total density with ρ_R and ρ_B being the densities of red and blue fluids, respectively; c_s is the speed of sound; $\boldsymbol{e}_\alpha$ is the lattice velocity in the αth direction, and w_α is the weight coefficient. For a two-dimensional nine-velocity (D2Q9) model used in this work, the speed of sound is defined as $c_s = \frac{c}{\sqrt{3}}$ with $c = \frac{\delta_t}{\delta_x}$, where δ_x is the lattice spacing and δ_t is the time step ($\delta_x = \delta_t$ is used hereafter); $\boldsymbol{e}_\alpha$ is defined as $\boldsymbol{e}_0 = (0,0), \boldsymbol{e}_{1,3} = (\pm 1, 0), \boldsymbol{e}_{2,4} = (0, \pm 1), \boldsymbol{e}_{5,6} = (\pm 1, 1), \boldsymbol{e}_{7,8} = (\mp 1, -1)$, and the weight factor is given by $w_0 = \frac{4}{9}, w_{1,2,3,4} = \frac{1}{9}, w_{5,6,7,8} = \frac{1}{36}$.

The transform matrix $\boldsymbol{M}$ in Eq.(2) is explicitly given by[39]

$$\boldsymbol{M}=\begin{bmatrix} 1 & 1 & 1 & 1 & 1 & 1 & 1 & 1 & 1 \\ -4 & -1 & -1 & -1 & -1 & 2 & 2 & 2 & 2 \\ 4 & -2 & -2 & -2 & -2 & 1 & 1 & 1 & 1 \\ 0 & 1 & 0 & -1 & 0 & 1 & -1 & -1 & 1 \\ 0 & -2 & 0 & 2 & 0 & 1 & -1 & -1 & 1 \\ 0 & 0 & 1 & 0 & -1 & 1 & 1 & -1 & -1 \\ 0 & 0 & -2 & 0 & 2 & 1 & 1 & -1 & -1 \\ 0 & 1 & -1 & 1 & -1 & 0 & 0 & 0 & 0 \\ 0 & 0 & 0 & 0 & 0 & 1 & 1 & 1 & -1 \end{bmatrix} \tag{4}$$

and the corresponding relaxation matrix is

$$\boldsymbol{S}=diag\left(\frac{1}{\tau_\rho},\frac{1}{\tau_e},\frac{1}{\tau_\varepsilon},\frac{1}{\tau_j},\frac{1}{\tau_q},\frac{1}{\tau_j},\frac{1}{\tau_q},\frac{1}{\tau_\upsilon},\frac{1}{\tau_\upsilon}\right) \tag{5}$$

where τ_ρ and τ_j are related to the conserved moments (i.e. mass and momentum), and can take any values. τ_υ is related to the kinematic viscosity υ by

$$\tau_\upsilon(\boldsymbol{x},t)=\frac{\upsilon(\boldsymbol{x},t)}{c_s^2\delta_t}+0.5 \tag{6}$$

The other relaxation times are related to the non-conserved moments and their values can be freely adjusted to enhance the stability of MRT model. In this paper, we choose, unless otherwise stated, the relaxation matrix as

$$\boldsymbol{S}=diag\left(1.0,1.64,1.54,1.0,1.9,1.0,1.9,\frac{1}{\tau_\upsilon},\frac{1}{\tau_\upsilon}\right) \tag{7}$$

The forcing term $\bar{F}_i$ in Eq. (1) contributes to the mixed interfacial region and creates an interfacial tension. In the MRT framework, the forcing term is given by

$$\overline{\boldsymbol{F}}=\boldsymbol{M}^{-1}(\boldsymbol{I}-0.5\boldsymbol{S})\boldsymbol{M}\widetilde{\boldsymbol{F}} \tag{8}$$

where $\boldsymbol{I}$ is a 9×9 unit matrix, $\overline{\boldsymbol{F}}=[\bar{F}_0,\bar{F}_1,\bar{F}_2,\cdots,\bar{F}_8]^T$, and $\widetilde{\boldsymbol{F}}=[\tilde{F}_0,\tilde{F}_1,\tilde{F}_2,\cdots,\tilde{F}_8]^T$. According to Guo et al.[40], $\widetilde{\boldsymbol{F}}_\alpha$ reads as

$$\tilde{F}_\alpha=w_\alpha\left[\frac{\boldsymbol{e}_\alpha-\boldsymbol{u}}{c_s^2}+\frac{(\boldsymbol{e}_\alpha\cdot\boldsymbol{u})\boldsymbol{e}_\alpha}{c_s^4}\right]\cdot\boldsymbol{F}\delta_t \tag{9}$$

where the interfacial force $\boldsymbol{F}$ is introduced based on the continuum surface force (CSF) method[41], and is expressed as

$$\boldsymbol{F}=\frac{1}{2}\sigma\kappa\boldsymbol{\nabla}\rho^N \tag{10}$$

In Eq. (10), σ is an interfacial tension coefficient, $\rho^N(\boldsymbol{x},t)$ is an indicator function, which is defined by the local densities of the red and blue fluids as

$$\rho^N(\boldsymbol{x},t) = \frac{\rho_R(\boldsymbol{x},t)-\rho_B(\boldsymbol{x},t)}{\rho_R(\boldsymbol{x},t)+\rho_B(\boldsymbol{x},t)} \tag{11}$$

and κ is the local interface curvature, which is calculated by

$$\kappa = -\boldsymbol{\nabla}_s \cdot \boldsymbol{n} \tag{12}$$

where $\boldsymbol{\nabla}_s = (\boldsymbol{I}-\boldsymbol{nn})\cdot\boldsymbol{\nabla}$ is the surface gradient operator, $\boldsymbol{n} = \frac{\boldsymbol{\nabla}\rho^N}{|\boldsymbol{\nabla}\rho^N|}$ is the interfacial unit normal vector pointing into the red fluid, and the local interface curvature in 2D can be written as

$$\kappa = -n_x^2\partial_y n_y - n_y^2\partial_x n_x + n_x n_y\left(\partial_y n_x + \partial_x n_y\right) \tag{13}$$

where n_x and n_y are the x- and y-component of the vector $\boldsymbol{n}$.

It can be shown using the Chapman-Enskog multi-scale analysis that, Eq. (1) along with Eqs. (2), (3), (8) and (9), can lead to the Navier-Stokes equations under the low Mach number limitation, and the pressure p and the fluid velocity are defined by

$$p(\boldsymbol{x},t) = \rho(\boldsymbol{x},t)c_s^2,\ \ \rho\boldsymbol{u}(x,t) = \textstyle\sum_\alpha f_\alpha(\boldsymbol{x},t)\boldsymbol{e}_\alpha + \frac{1}{2}\boldsymbol{F}(\boldsymbol{x},t)\delta_t \tag{14}$$

To promote phase segregation and maintain a reasonable interface, the recoloring algorithm proposed by Latva-Kokko and Rothman[23] is then applied. It is beneficial to further reduce spurious velocities at the interface and overcome the lattice pinning problem. Following this algorithm, the recolored distribution functions of red and blue fluids, i.e. $f''_{\alpha,R}$ and $f''_{\alpha,B}$, are given as

$$\begin{aligned} f''_{\alpha,R}(\boldsymbol{x},t) &= \frac{\rho_R}{\rho}f'_\alpha(\boldsymbol{x},t) + \beta\frac{\rho_R\rho_B}{\rho}w_i\frac{\boldsymbol{e}_\alpha\cdot\boldsymbol{\nabla}\rho^N}{|\boldsymbol{\nabla}\rho^N|} \\ f''_{\alpha,B}(\boldsymbol{x},t) &= \frac{\rho_B}{\rho}f'_\alpha(\boldsymbol{x},t) - \beta\frac{\rho_R\rho_B}{\rho}w_\alpha\frac{\boldsymbol{e}_\alpha\cdot\boldsymbol{\nabla}\rho^N}{|\boldsymbol{\nabla}\rho^N|} \end{aligned} \tag{15}$$

where β is a segregation parameter related to the interface thickness and is set to be 0.7 for numerical stability and model accuracy[35].

After the recoloring step, the streaming step for both the red and blue distribution functions is performed, i.e.

$$f_{\alpha,k}(\boldsymbol{x}+\boldsymbol{e}_\alpha\delta_t, t+\delta_t) = f''_{\alpha,k}(\boldsymbol{x},t), \quad k = R\ or\ B \tag{16}$$

With the post-streaming distribution functions, the density of each fluid is calculated by

$$\rho_k = \sum_\alpha f_{\alpha,k}, \quad k = R \; or \; B \tag{17}$$

In this work, both immiscible fluids are assumed to have equal densities for the sake of simplicity. To account for unequal viscosities of both fluids, a harmonic mean[42] is adopted in the interfacial region to determine the viscosity μ of the fluid mixture, i.e.

$$\frac{1}{\mu(\rho^N)} = \frac{1+\rho^N}{2\mu_R} + \frac{1-\rho^N}{2\mu_B} \tag{18}$$

where μ_R and μ_B are the dynamic viscosities of the red and blue fluids, respectively.

Interfacial force condition in contact line region

A zero-interfacial-force condition in contact line region is first demonstrated based on the diffuse interface model. We then describe how such a condition is appropriately implemented in the present color-gradient LBM, where the interface is typical of diffuse nature. Without loss of generality, we consider two immiscible fluids adhering to a horizontal surface, which is illustrated in Figure 1. For the point P in the contact line region, the unit normal vector of the solid surface is $\boldsymbol{n}_s$, and the color gradient function is $\boldsymbol{\nabla}\rho^N$, which points into the red fluid. To achieve the desired contact angle θ, it is required that the angle between the vectors $\boldsymbol{n}_s$ and $\boldsymbol{\nabla}\rho^N$ is equal to θ (which is known as the contact angle condition). As shown in the right panel of Figure 1, there are two states of the interface to meet this requirement, which correspond to two different directions of $\boldsymbol{\nabla}\rho^N$. To distinguish the directions of $\boldsymbol{\nabla}\rho^N$, we define the intersection angles as follows: $\theta = \theta_+$ if the vector $\boldsymbol{\nabla}\rho^N$ is in the clockwise direction of $\boldsymbol{n}_s$; otherwise, $\theta = \theta_-$. Therefore, one can obtain the relationship between $\partial_x\rho^N$ and $\partial_y\rho^N$ in the contact line region, which reads

$$\partial_y\rho^N = f(\theta)\partial_x\rho^N \tag{19}$$

where

$$f(\theta) = \begin{cases} \cot\theta, & \theta = \theta_+ \\ -\cot\theta, & \theta = \theta_- \end{cases} \tag{20}$$

Note that in Eq. (19) the sign of $\partial_x\rho^N$ is determined by the direction of the intersection angle θ (i.e. clockwise or counter-clockwise):

$$\begin{cases} \partial_x\rho^N < 0, & \theta = \theta_+ \\ \partial_x\rho^N > 0, & \theta = \theta_- \end{cases} \tag{21}$$

In a 2D case, the interfacial unit normal vector can be written as

$$\boldsymbol{n} = \frac{\boldsymbol{\nabla}\rho^N}{|\boldsymbol{\nabla}\rho^N|} = P(x,y)\partial_x\rho^N\boldsymbol{i} + P(x,y)\partial_y\rho^N\boldsymbol{j} = n_x\boldsymbol{i} + n_y\boldsymbol{j} \tag{22}$$

where $P(x,y) = \frac{1}{\sqrt{(\partial_x \rho^N)^2 + (\partial_y \rho^N)^2}}$, and $\boldsymbol{i}$ and $\boldsymbol{j}$ are the unit vectors in the x- and y-direction, respectively.

Considering the first state $\theta = \theta_+$ in the contact line region, we have

$$P(x,y) = -\frac{1}{\partial_x \rho^N} \frac{1}{\sqrt{1+(\cot\theta)^2}} = -\frac{\sin\theta}{\partial_x \rho^N} \tag{23}$$

where Eq. (19) is used. Furthermore, the derivatives of $P(x,y)$ can be calculated, i.e.

$$\begin{aligned} \partial_x P &= \frac{\sin\theta}{(\partial_x \rho^N)^2} \partial_x^2 \rho^N \\ \partial_y P &= \frac{\sin\theta}{(\rho^N)^2} \partial_y \partial_x \rho^N \end{aligned} \tag{24}$$

Combination of Eqs. (24) and (22) leads to

$$\begin{aligned} \partial_x n_x &= -\frac{\sin\theta}{\partial_x \rho^N} \cdot \partial_x{}^2 \rho^N + \frac{\sin\theta}{(\partial_x \rho^N)^2} \partial_x{}^2 \rho^N \cdot \partial_x \rho^N = 0 \\ \partial_y n_x &= -\frac{\sin\theta}{\partial_x \rho^N} \cdot \partial_y \partial_x \rho^N + \frac{\sin\theta}{(\partial_x \rho^N)^2} \partial_y \partial_x \rho^N \cdot \partial_x \rho^N = 0 \\ \partial_x n_y &= -\frac{\sin\theta}{\partial_x \rho^N} \cdot \partial_x (\partial_x \rho^N \cot\theta) + \frac{\sin\theta}{(\partial_x \rho^N)^2} \partial_x{}^2 \rho^N \cdot (\partial_x \rho^N \cot\theta) = 0 \\ \partial_y n_y &= -\frac{\sin\theta}{\partial_x \rho^N} \cdot \partial_x{}^2 (\rho^N (\cot\theta)^2) + \frac{\sin\theta}{(\partial_x \rho^N)^2} \partial_x (\partial_x \rho^N \cot\theta) \cdot (\partial_x \rho^N \cot\theta) = 0 \end{aligned} \tag{25}$$

Similarly, considering the other state $\theta = \theta_-$ in a similar manner, we also obtain

$$\partial_x n_x = \partial_y n_x = \partial_x n_y = \partial_y n_y = 0 \tag{26}$$

Substituting Eqs. (25) and (26) into Eq. (10), we can obtain

$$\boldsymbol{F}(\boldsymbol{x}) = \boldsymbol{0} \tag{27}$$

for $\boldsymbol{x}$ in the contact line region. This is known as zero-interfacial-force condition which is inherent to diffuse interface models and should be properly enforced in our wetting boundary treatment.

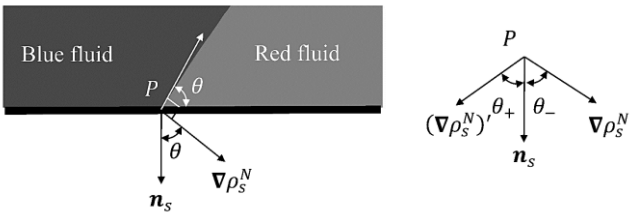

Figure 1. Illustration of the relationship between the normal of solid surface and the color gradient in contact line region.

Generalized wetting boundary treatment

Here, we present a generalized wetting boundary treatment, which is applicable to arbitrarily complex solid surfaces. In the present model, the gradients $\nabla\rho^N$ and ∇n_i need to be evaluated, where the subscript $i = x\ or\ y$ in a 2D case. To facilitate the description of wetting boundary treatment, the lattice nodes are divided into several different categories, i.e.
Ω_F: a list of the fluid nodes;
Ω_S: a list of the solid nodes;
Ω_{FB}: a list of the fluid nodes that are in contact with at least one solid node;
Ω_{FI}: a list of the fluid nodes that are not in contact with any solid nodes;
Ω_{SB}: a list of the solid nodes that are in contact with at least one fluid node;
Ω_{SI}: a list of the solid nodes that are not in contact with any fluid nodes.

For the lattice nodes in Ω_{FI}, we use a fourth-order isotropic finite difference to evaluate the gradient of a variable φ, which is given by

$$\partial_i\varphi(\boldsymbol{x}) = \frac{1}{c_s^2\delta_t}\sum_\alpha w_\alpha\varphi(\boldsymbol{x}+\boldsymbol{e}_\alpha\delta_t)\boldsymbol{e}_{\alpha i} \tag{28}$$

where $\varphi(\boldsymbol{x})$ refers to ρ^N, n_x, and n_y. However, for the lattice nodes $\boldsymbol{x}$ in Ω_{FB}, Eq. (28) cannot be directly applied to the gradient calculations since the values of ρ^N, n_x and n_y are unknown on the neighboring solid nodes (i.e. $\boldsymbol{x}+\boldsymbol{e}_\alpha\delta_t \in \Omega_{SB}$). To extend the use of Eq. (28) to the lattice nodes in Ω_{FB}, one needs to first evaluate ρ^N, n_x and n_y on the lattice nodes in Ω_{SB} so that both the contact angle condition and the zero-interfacial-force condition $\nabla n_i = 0$, are appropriately imposed in the contact line region.

Contact angle condition

We follow Xu et al.[42] to impose the contact angle condition, in which the key is to construct the color gradient $\nabla\rho^N$ at the contact lines so that it matches the desired contact angle θ. As mentioned above, the value of ρ^N in Ω_{SB} is unknown but required in order to compute $\nabla\rho^N$ in Ω_{FB} using Eq. (28). Thus, we first evaluate the value of ρ^N in Ω_{SB} through a weighted average of its nearest ρ^N in Ω_{FB}, which is given by

$$\rho^N(\boldsymbol{x}) = \frac{\sum_{\alpha_1} w_{\alpha_1}\rho^N(\boldsymbol{x}+\boldsymbol{e}_{\alpha_1}\delta_t)}{\sum_{\alpha_1} w_{\alpha_1}},\ \ \boldsymbol{x}\in\Omega_{SB} \tag{29}$$

where the subscript α_1 is the α_1th lattice velocity direction which satisfies $\boldsymbol{x}+e_{\alpha_1}\delta_t \in \Omega_{FB}$. With the values of ρ^N obtained from Eq. (29), we are able to compute the color gradient in Ω_{FB}, which, however, does not necessarily match the desired contact angle (actually, it will be shown shortly that Eq. (29) leads to $\boldsymbol{n}_s\cdot\nabla\rho^N = 0$, which gives a constant contact angle of 90°). Thus, such a color gradient is only considered as a predicted one (denoted by $\nabla\rho^{N*}$, and the corresponding direction is $\boldsymbol{n}^* = \frac{\nabla\rho^{N*}}{|\nabla\rho^{N*}|}$), which needs to be modified. The principle of the modification is to adjust the direction of the color gradient $\nabla\rho^{N*}$ in Ω_{FB} while keeping its modulus $|\nabla\rho^{N*}|$unchanged. Assuming at contact lines that the unit normal vector of the interface is properly determined and is given by $\boldsymbol{n}_f$, the modified color gradient ρ^N is obtained by

$$\nabla\rho^N = |\nabla\rho^{N*}|\boldsymbol{n}_f \tag{30}$$

When complex geometries such as porous media are considered, the properties of pixels or nodes are generally given instead of the shape and the curvature of solid surfaces. With the given properties of nodes (either solid or fluid), the unit normal vector $\boldsymbol{n}_s$ of solid surface can be calculated by an eighth-order isotropic finite difference, which is given by[42]

$$\boldsymbol{n}_s(\boldsymbol{x}) = \frac{\sum_k w(|\boldsymbol{c}_k|^2)s(\boldsymbol{x}+\boldsymbol{c}_k\delta_t)\boldsymbol{c}_k}{|\sum_k w(|\boldsymbol{c}_k|^2)s(\boldsymbol{x}+\boldsymbol{c}_k\delta_t)\boldsymbol{c}_k|}, \quad \boldsymbol{x} \in \Omega_{FB} \tag{31}$$

where $\boldsymbol{c}_k$ is the kth mesoscopic velocity of the eighth-order isotropic discretization as presented in the work of Sbragaglia et al.[43], $s(\boldsymbol{x})$ is an indicator function which equals 0 for $\boldsymbol{x} \in \Omega_F$ and 1 for $\boldsymbol{x} \in \Omega_S$, and $w(|\boldsymbol{c}_k|^2)$ is the eighth-order weight coefficient given[43] by

$$w(|\boldsymbol{c}_k|^2) = \begin{cases} \frac{4}{21} & |\boldsymbol{c}_k|^2 = 1 \\ \frac{4}{45} & |\boldsymbol{c}_k|^2 = 2 \\ \frac{1}{60} & |\boldsymbol{c}_k|^2 = 4 \\ \frac{2}{315} & |\boldsymbol{c}_k|^2 = 5 \\ \frac{1}{5040} & |\boldsymbol{c}_k|^2 = 8 \end{cases} \tag{32}$$

As stated before, there are two possible theoretical directions of $\nabla\rho^N$ (i.e. unit normal vectors of the interface) at the contact lines for a given contact angle θ. These two directions, denoted as $\boldsymbol{n}_{f1}$ and $\boldsymbol{n}_{f2}$, are obtained by rotating $\boldsymbol{n}_s$ with an angle θ in the clockwise and counterclockwise directions, respectively (see Figure 1). The resulting $\boldsymbol{n}_{f1}$ and $\boldsymbol{n}_{f2}$ are

$$\begin{aligned} \boldsymbol{n}_{f1} &= \left(n_{sx}\cos\theta - n_{sy}\sin\theta\,, n_{sy}\cos\theta + n_{sx}\sin\theta\right) \\ \boldsymbol{n}_{f2} &= \left(n_{sx}\cos\theta + n_{sy}\sin\theta\,, n_{sy}\cos\theta - n_{sx}\sin\theta\right) \end{aligned} \tag{33}$$

where n_{sx} and n_{sy} are the x- and y-component of $\boldsymbol{n}_s$. As previously done by Leclaire et al.[24], the Euclidean distances D_1 and D_2 are used to choose an appropriate theoretical direction, which are defined by

$$D_1 = \left|\boldsymbol{n}_{f1} - \boldsymbol{n}^*\right|, \quad D_2 = \left|\boldsymbol{n}_{f2} - \boldsymbol{n}^*\right| \tag{34}$$

and the unit normal vector of the interface $\boldsymbol{n}_f$ is then selected by

$$\boldsymbol{n}_f = \begin{cases} \boldsymbol{n}_{f1} & D_1 \le D_2 \\ \boldsymbol{n}_{f2} & D_1 > D_2 \end{cases} \tag{35}$$

Zero-interfacial-force condition

As derived before, the zero-interface-force condition, i.e. $\nabla n_i = 0$, should be satisfied in the contact line region. In the curvature evaluation, we propose to first introduce the virtual values of n_i on the lattice

nodes $\boldsymbol{x} \in \Omega_{SB}$ through Eq. (29), and then calculate $\boldsymbol{\nabla} n_i$ in $\boldsymbol{x} \in \Omega_{FB}$ through Eq. (28). It is shown below that the zero-interfacial-force condition can be exactly achieved by such a simple implementation.

The weighted-average virtual scheme given by Eq. (29) can be rewritten as

$$\sum_{\alpha_1} w_{\alpha_1} \left[\varphi\left(\boldsymbol{x} + \boldsymbol{e}_{\alpha_1}\right) - \varphi(\boldsymbol{x})\right] = 0 \tag{36}$$

where $\varphi = n_i$. Using the Taylor expansion and discarding the second- and higher-order residual terms, we have

$$\sum_{\alpha_1} w_{\alpha_1} e_{\alpha_1 i}\, \partial_i \varphi(\boldsymbol{x}) = 0 \tag{37}$$

Let

$$\boldsymbol{a} = \sum_{\alpha_1} w_{\alpha_1}\, e_{\alpha_1 i} \tag{38}$$

$$\boldsymbol{b} = \partial_i \varphi(\boldsymbol{x}) \tag{39}$$

Obviously $\boldsymbol{a} \neq \boldsymbol{0}$, so Eq. (37) gives

$$\boldsymbol{b} = \boldsymbol{0} \; or \; \boldsymbol{b} \perp \boldsymbol{a} \tag{40}$$

where $\boldsymbol{a}$ is simply regarded as the normal vector of the solid surface, so $\boldsymbol{b} = \partial_i \varphi(\boldsymbol{x})$ should be in the tangential direction of the solid surface when $\boldsymbol{b} \neq \boldsymbol{0}$. In either case, we have

$$\boldsymbol{n}_s \cdot \nabla \varphi(\boldsymbol{x}) = 0 \tag{41}$$

which leads to $\partial_y \varphi(x) = 0$ for the horizontal surface shown as in Figure 1. From Eqs. (19) and (22), one can easily derive the relationship between two components of the gradient ∇n_i, which is given by

$$\partial_y n_i = f(\beta) \partial_x n_i \tag{42}$$

Combining $\partial_y \varphi(x) = 0$ and Eq. (42), we get to

$$\boldsymbol{\nabla} n_i = 0 \tag{43}$$

Numerical simulations

To validate the present color-gradient model, four typical cases are to be considered, including two static problems, i.e. a static droplet on a flat surface and a cylindrical surface, as well as two dynamic problems, i.e. capillary filling and immiscible displacement in a channel. In our simulations of the static problems, the convergence criterion is selected as

$$E_1 = max\left(\left|u_x^{t+500} - u_x^t\right|, \left|u_y^{t+500} - u_y^t\right|\right) < 10^{-7} \tag{44}$$

and we calculate the maximum value of spurious velocities by

$$|\boldsymbol{u}|_{max} = max\left(\sqrt{u_x^2 + u_y^2}\right) \tag{45}$$

Meanwhile, the NPMT effect in static problems is quantified by[24]

$$E_{NPMT} = \sqrt{\left(\frac{m_R^{inc}}{m_R^{all}}\right)^2 + \left(\frac{m_B^{outc}}{m_B^{all}}\right)^2} \tag{46}$$

where m_R (m_B) is the nominal mass of the red (blue) fluid, calculated by the summation of ρ_R (ρ_B) in a certain region; the superscripts $inc, outc, all$ denote the regions inside the circle C (note that C is a theoretical phase interface), outside the circle C, and in the entire computational domain respectively.

A static droplet on a flat surface

In this part, simulations are performed in a 160×100 lattice domain. Initially, a circle segment-shaped droplet with the radius $R = 45$ is placed on the bottom wall. The center of the droplet is $(x_c, y_c) = \left(\frac{160}{2}, \frac{3}{2} - R\cos\theta\right)$, which depends on the contact angle θ at the bottom wall. The interfacial tension parameter is $\sigma = 0.02$, and two different viscosity ratios $\left(M = \frac{\upsilon_R}{\upsilon_B}\right)$ are investigated with $\upsilon_R = 0.35$. Although the periodic boundary conditions can offset the NPMT effect to some extent[24], this offset does not exist in most practical applications. We therefore choose a closed computational domain with all the boundaries being no-slip walls. Table 1 shows the simulated angles at both M=1 and M=100, which are calculated by the droplet height h and the wet length l between the droplet and the bottom wall as[44]: $\tan(\theta) = l/(l^2/4h - h)$. All the simulated results agree well with the theoretical ones, but the simulated results at M=100 are closer to the theoretical values. In addition, it is observed in Table 2 that the spurious velocities are suppressed to a significantly low level. Specifically, the maximum spurious velocities are on the order of $O(10^{-4})$ or smaller at M=1, and on the order of $O(10^{-3})$ or smaller at M=100. Larger spurious velocities at M=100 can be explained as follows. The appearance of spurious velocities is to generate viscous forces that compensate the imbalanced pressure and interfacial tension force. According to the definition of viscous force, i.e. $\nabla \cdot [\mu(\nabla \boldsymbol{u} + \nabla \boldsymbol{u}^{\mathrm{T}})]$, a smaller fluid viscosity always requires larger velocities to achieve the same viscous forces. A larger viscosity ratio corresponds to a smaller viscosity of the blue fluid, so the spurious velocities are larger at M=100 than at M=1.

Table 1. Simulated contact angles at both M=1 and M=100 for a droplet on a flat surface.

M	30°	60°	90°	120°	150°
1	30.96	60.20	90.05	120.18	151.77
100	29.99	60.01	90.00	120.09	151.02

Table 2. Maximum spurious velocities at both M=1 and M =100 for various contact angles. All the values of the velocity are magnified by 10^{-4} times.

M	30°	60°	90°	120°	150°
1	1.79	0.51	0.18	0.59	1.47
100	33.4	11.9	1.86	6.29	10.3

In the color-gradient model, several strategies have been developed to implement the wetting boundary condition, e.g. the commonly-used "virtual color method" which imposes the virtual color value $\rho^N = \cos\theta$ on the lattice nodes $\boldsymbol{x} \in \Omega_{SB}$ in order to obtain the desired contact angle θ[45], and the geometric formulation method, which first evaluates the tangential component of the color gradient at wall surfaces and then computes the normal component using the contact angle geometric formulation

proposed by Ding and Spelt[26]. It should be noted that the original geometric formulation method suffers from the difficulty of dealing with curved solid boundaries. We run the simulations with the wetting boundary condition imposed by the present method, the virtual color method, and the original geometric formulation method. The viscosity ratio is fixed as $M = 1$, and the contact angle is set as $30^{\circ}, 60^{\circ}, 90^{\circ}, 120^{\circ}, 150^{\circ}$. Figure 2 shows the time evolution of E_{NPMT} obtained by different methods at various contact angles. It is clearly seen that, for each of contact angles considered, E_{NPMT} obtained by the present method is always the smallest, and it quickly reaches a constant value after an initial increase. This suggests that the present method can effectively suppress the NPMT, thereby leading to more convincing results.

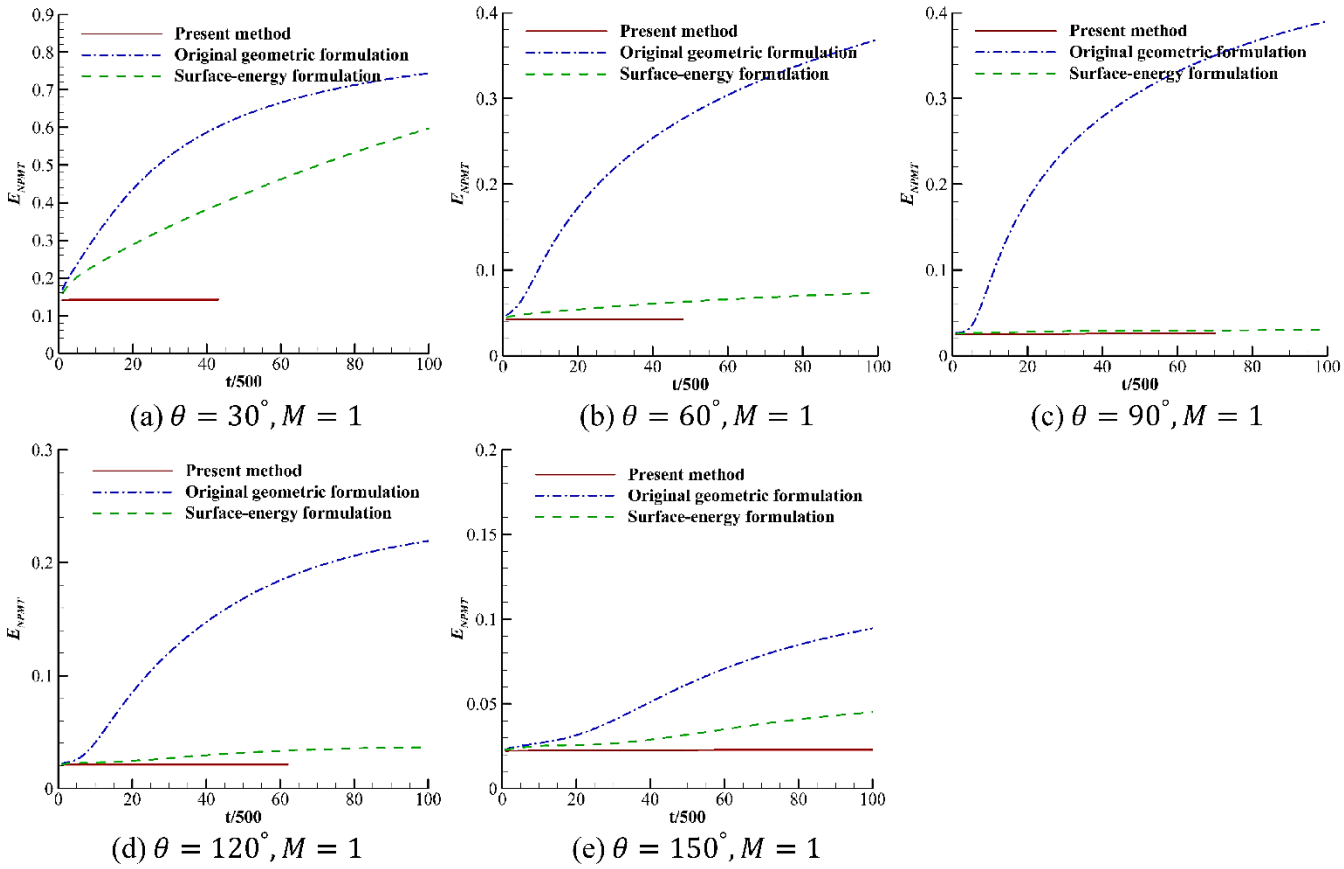

Figure 2. The evolution of E_{NPMT} obtained with the present method (solid lines), the original geometric formulation method (dashed lines) and the virtual color method (dash-dot lines) at different contact angles.

A static droplet on a cylindrical surface

To test the present model's capability in handing curved boundary problems, we simulate a droplet resting on a cylindrical surface in a 200×200 lattice domain. The solid cylinder and the droplet are centered at $(100, 60)$ and $(100, 2R \sin\theta + 60)$ respectively, and their radii are both set as $R = 40$. The viscosity ratio of both fluids is fixed at 1, and a broad range of contact angles, i.e. $10^{\circ}, 30^{\circ}, 45^{\circ}, 60^{\circ}, 90^{\circ}, 120^{\circ}, 135^{\circ}, 150^{\circ}, 170^{\circ}$ are considered. The simulations are run until the system reaches the steady state, and the results are displayed in Figure 3. For each of the contact angles considered, the simulated result overall agrees well with the theoretical prediction which is represented by the dash-dot circle. However, it is worth noting that, when the contact angle is not less than 150°, the

simulated droplet is positioned slightly above the theoretical profile. It is caused by the insufficient grid resolution in the contact region between the solid surface and the red fluid, which is even smaller than the interface thickness. The maximum spurious velocities for all the contact angles are shown in Table 3, which are on the orders of 10^{-5} to 10^{-4}. These results indicate that the proposed wetting boundary treatment is appropriate for complex solid surfaces, producing good numerical accuracy for various contact angles and low spurious velocities.

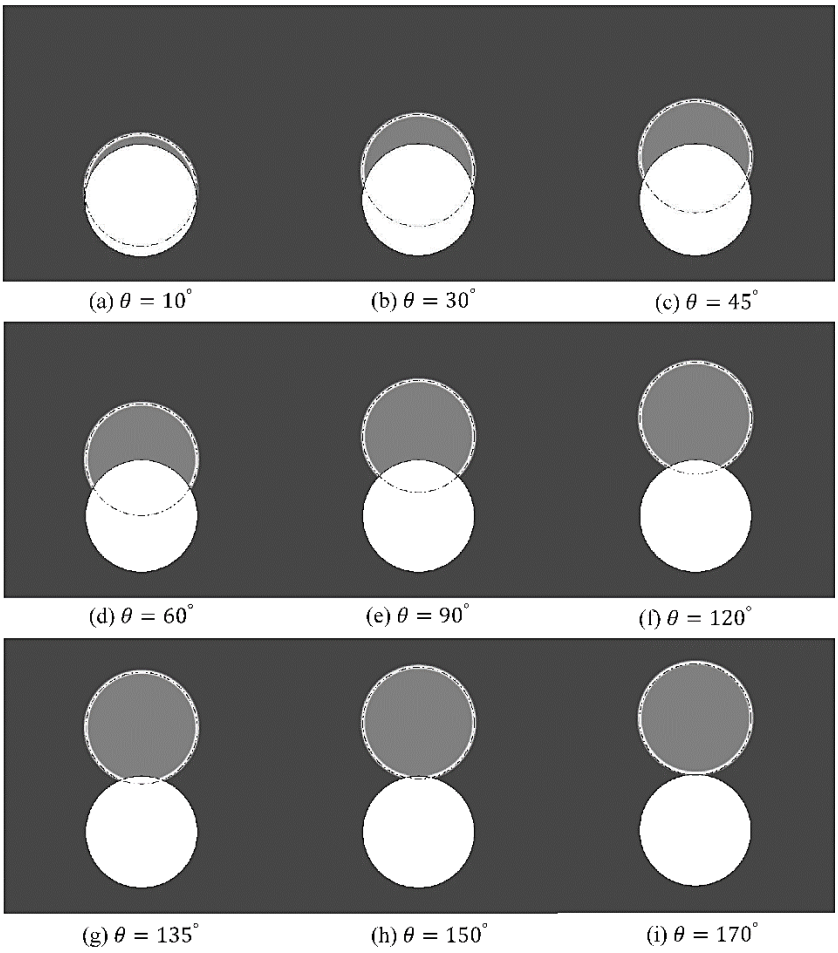

Figure 3. A droplet resting on a cylindrical surface with different contact angles. Note that the red and blue fluids are shown in light gray and dark gray, respectively.

Table 3. The maximum spurious velocities at various contact angles for a droplet resting on a cylindrical surface.

θ	10°	30°	45°	60°	90°	120°	135°	150°	170°
$\lvert \boldsymbol{u} \rvert_{max} \times 10^5$	1.51	1.19	1.40	2.26	6.10	16.5	22.4	30.6	26.5

It was suggested by Xu et al.[42] to use the eighth-order isotropic discretization to estimate the unit normal vector $\boldsymbol{n}_s$ of solid surface. For the present problem, the unit normal vector of the solid surface is calculated by the eighth-order isotropic discretization (see Eq. (31)) or directly designated as the theoretical unit normal vector of the cylindrical surface, which are referred to as "8th-order discretization" and "theoretical designation", respectively. Here we conduct the simulations to study how the eighth-order isotropic discretization influences the numerical results. Five different contact angles, i.e. $30^{\circ}, 60^{\circ}, 90^{\circ}, 120^{\circ}, 150^{\circ}$, are considered, and all the other parameters are kept the same as those in Figure 3. Table 4 shows the maximum spurious velocities and E_{NPMT} obtained by the 8th-oder discretization and the theoretical designation. Compared with the 8th-oder discretization, the theoretical designation usually has smaller spurious velocities, especially when the contact angle is relatively small. On the other hand, both treatments produce almost the same values of E_{NPMT}, suggesting that the eighth-order isotropic discretization is accurate enough for the calculation of $\boldsymbol{n}_s$.

Table 4. The maximum spurious velocities and E_{NPMT} obtained by two different treatments for the unit normal vector of the solid surface, i.e. the 8th-order discretization and the theoretical designation.

	$\lvert\boldsymbol{u}\rvert_{max} \times 10^4$		$E_{NPMT} \times 10^2$	
θ	8th-order discretizaiton	Theoretical designation	8th-order discretizaiton	Theoretical designation
30°	3.56	0.12	3.55	4.44
60°	1.36	0.23	2.72	2.70
90°	0.65	0.61	2.36	2.23
120°	2.21	1.65	2.32	2.32
150°	4.89	3.07	2.93	2.76

Capillary filling

Capillary filling is a typical benchmark case for assessing whether a two-phase model is able to simulate moving contact line problems[4]. The velocity of a wetting fluid column filling a capillary tube of length L and width W, as shown in Figure 4, is determined by the capillary pressure and the viscous pressure drop. When the gravity and inertial effects can be neglected, this force balance can be expressed as[4, 46]

$$\sigma \cos\theta = \frac{6}{d}[\mu_R x + \mu_B (L - x)]\frac{dx}{dt} \tag{47}$$

where σ is fixed at 5×10^{-3}, θ is the contact angle which is $10^{\circ}, 30^{\circ}, 45^{\circ}, 60^{\circ}$ for the wetting (red) fluid, and x is the position of the moving interface with $x = 0$ at the inlet of capillary tube. The system consists of a 400×35 lattice domain with periodic boundary conditions used in the x-direction. The capillary tube is positioned in the middle, i.e. $100 \le x \le 300$ (which gives the length of capillary tube $L = 200$), with a thickness of 7 lattice grids. Outside of the middle portion, the boundary conditions are periodic in the y-direction, mimicking an "infinite reservoir". In the fluid domain, the blue fluid is initialized at the positions $120 \le x \le 375$, and the remaining lattice sites are filled with the red fluid. Two different viscosity ratios $M = 1$ and $M = 100$ are simulated, which are obtained by adjusting $\upsilon_B = \frac{\upsilon_R}{M}$ whilst keeping $\upsilon_R = 0.35$. Figure 5 shows the time evolution of the interface position x for different contact angles at (a) $M = 1$ and (b) $M = 100$, which is compared with the results from the method of Leclaire et al.[24] and the theoretical prediction from Eq. (47). It is clear that our simulated results agree better with the theoretical predictions than those obtained by the method of Leclaire et al.[24].

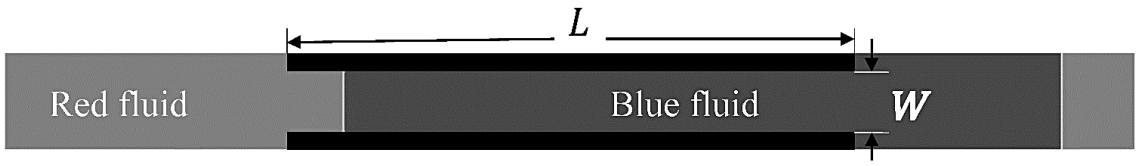

Figure 4. Geometry and initialization of the capillary filling problem. The portion in the center of the domain is a capillary tube of length L and width W. The red fluid is wetting with respect to the tube while the blue fluid is non-wettting.

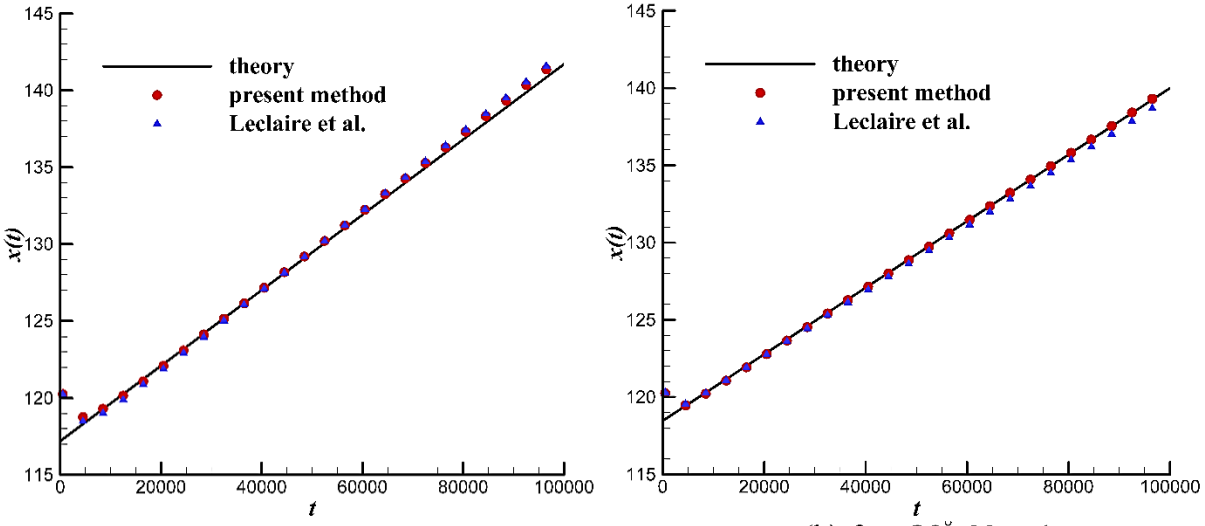

(a) $\theta = 10^{\circ}, M = 1$ (b) $\theta = 30^{\circ}, M = 1$

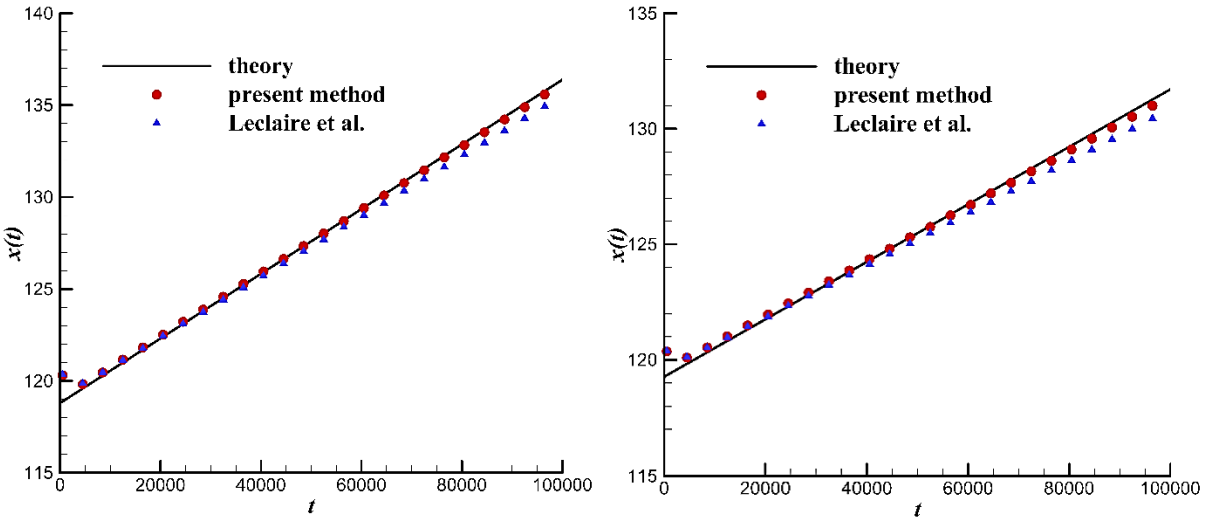

(c) $\theta = 45^{\circ}, M = 1$ (d) $\theta = 60^{\circ}, M = 1$

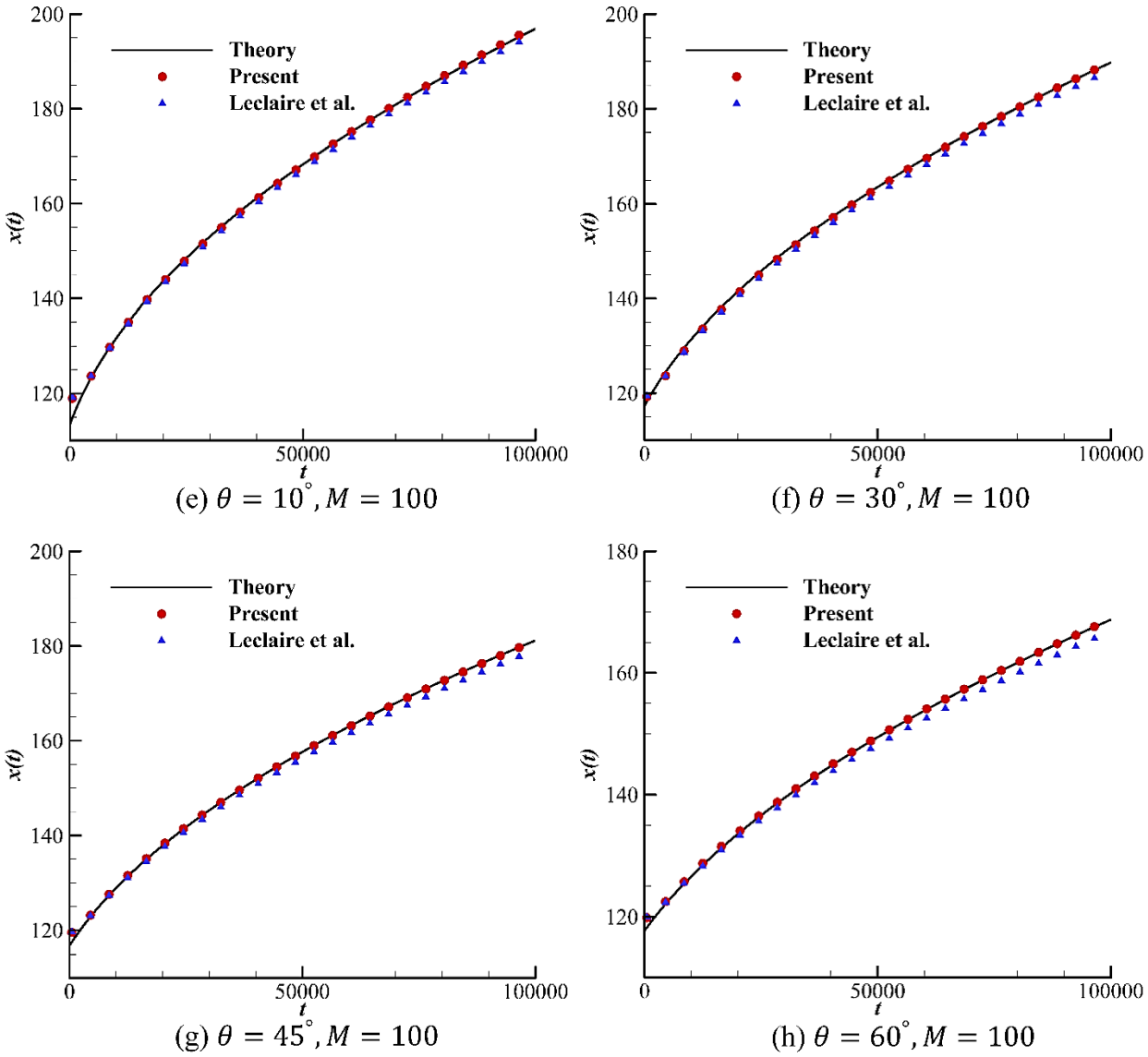

Figure 5. Time evolution of the interface position $x(t)$, for different contact angles at the viscosity ratios of (a) $M = 1$ and (b) $M = 100$. The black solid lines are the theoretical predictions from Eq. (47); the red squares represent the simulated results of the present method, while the blue triangles represent the simulated results from the method of Leclaire et al.[24].

Displacement of immiscible fluids in a channel

The displacement of immiscible fluids in a 2D channel is able to offer the first-hand knowledge regarding preferential flow through porous media that plays a tremendously important role in environmental science and reservoir engineering. It has been previously studied by Chin et al.[47], Kang et al.[48], Dong et al.[49] and Shi et al.[50] using different multiphase LBM models. Among these works, the pseudopotential model was used except the work of Shi et al.[50]. However, for the pseudopotential model, the interfacial tension parameter cannot be tuned flexibly since it is related to the miscibility, and the viscosity and density ratios of both fluids. In addition, the viscosity ratio is usually limited to less than 10 in the pseudopotential model because of numerical instability. By exploiting the present color-

gradient model, we can systematically investigate the effects of capillary number, viscosity ratio, and surface wettability on the two-phase displacement in a 2D channel, complementary to the previous studies based on a strictly verified wetting boundary scheme.

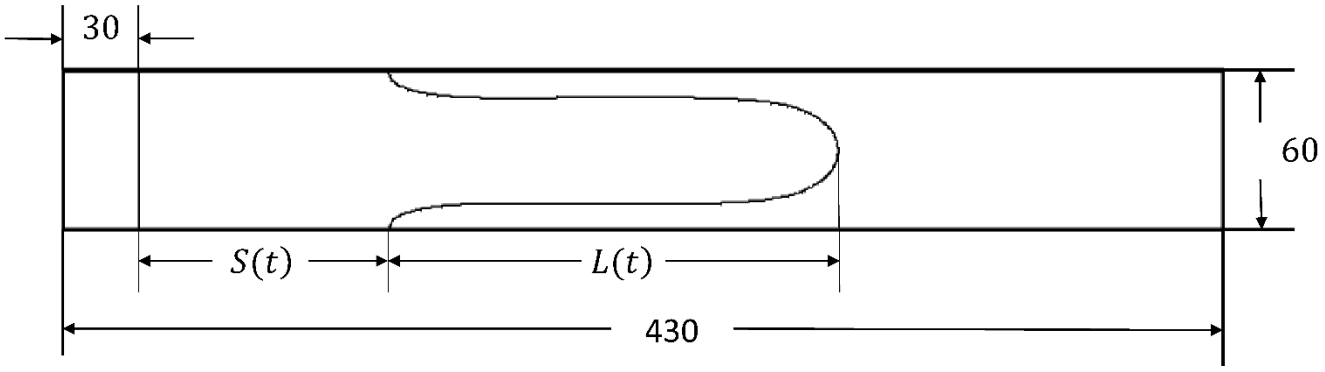

Figure 6. Schematic illustration of simulation geometry.

The simulations are performed in a 430×60 lattice domain, and the initial interface is located at $x = 30$ so that the curved interface remains in the computational domain during all the simulations. The displacing (red) fluid is injected continuously from the left inlet, where a Poiseuille velocity profile with the maximum velocity $u_0 = 0.01$ is specified following Zou and He[51]; on the right outlet, a constant pressure boundary condition is employed. The top and bottom walls are no-slip with the proposed wetting boundary condition imposed on them. Three parameters are used to quantify the interface movement: $S(t)$ is the moving distance of the contact line relative to the initial position, i.e. $S(t_0) = 0$, $L(t)$ is the finger length which is measured at the horizontal center line of the channel, and L_{eq} is the equilibrium finger length. The displacement behavior in a channel is governed by several important parameters, including the contact angle θ of the displacing fluid, the capillary number $Ca = \frac{\upsilon_B u_0}{\sigma}$, and the viscosity ratio of the displaced fluid to the displacing fluid ($M = \frac{\upsilon_B}{\upsilon_R}$).

Effects of capillary number and viscosity ratio

The effects of capillary number Ca and viscosity ratio M are investigated here. Figure 7 shows the evolution of interface morphologies at the viscosity ratio of unity for different capillary numbers: (a) $Ca = 0.1$, (b) $Ca = 0.2$, (c) $Ca = 0.4$, and (d) $Ca = 0.8$. It is clear that the simulated results basically match with those from the previous studies in morphologies.

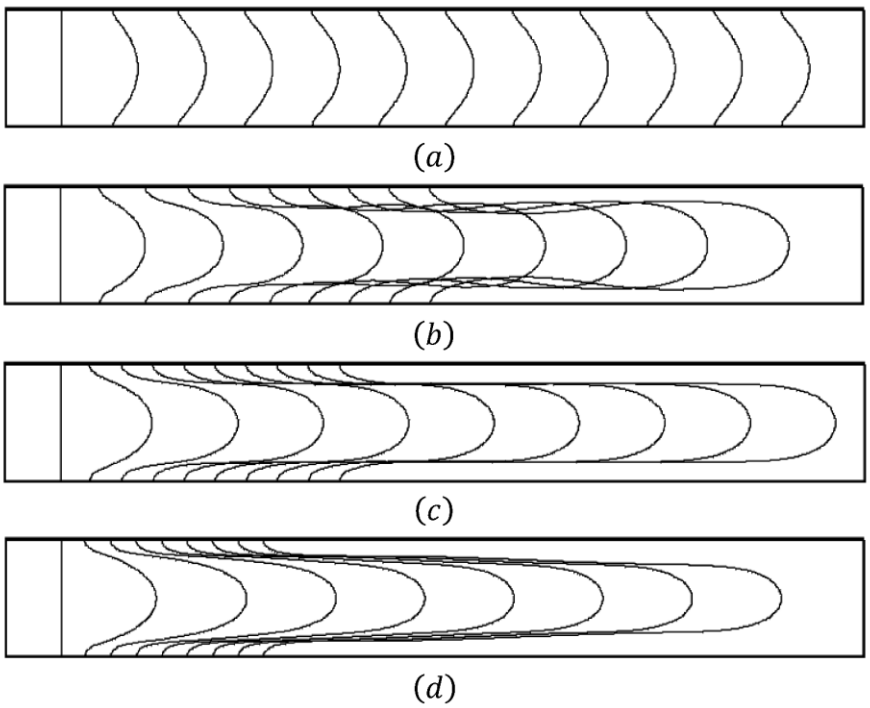

Figure 7. The evolution of interface morphologies for $M = 1$, $v_B = 0.48$, $u_0 = 0.01$, $\Delta t = 5 \times 10^3$, $\theta = 90^\circ$ with (a) $Ca = 0.1$, (b) $Ca = 0.2$, (c) $Ca = 0.4$ and (d) $Ca = 0.8$.

To quantitatively analyze the behavior of viscous displacement, Ca is taken as 0.1, 0.2, 0.4 and 0.8; M is varied from 1 to 200 whilst keeping $v_B = 0.48$; u_0 fixed at 0.01, and the contact angle $\theta = 90^\circ$. When the interface movement reaches the steady state, we compute $\frac{dS}{dt}$, $\frac{dL}{dt}$ and L_{eq}, which are plotted in Figure 8.

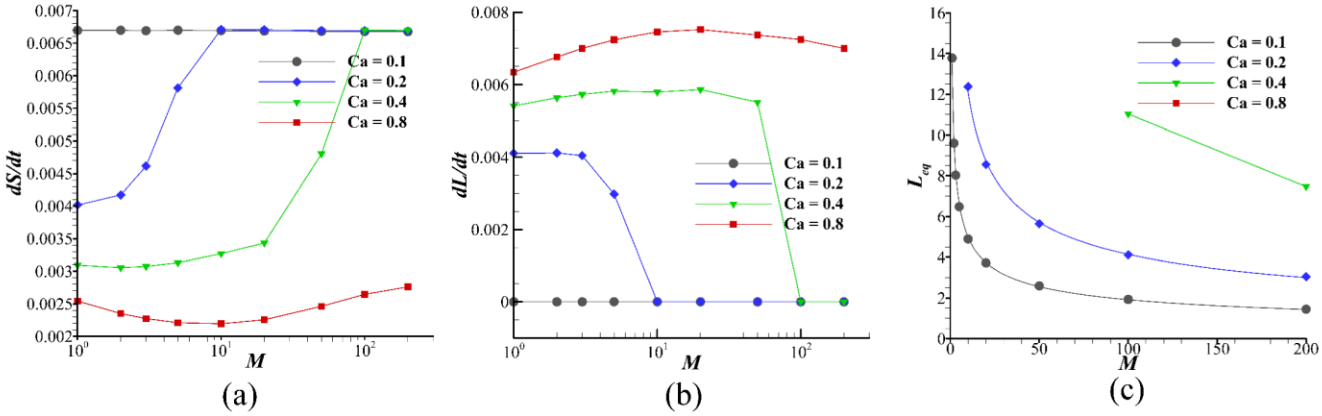

Figure 8. (a) $\frac{dS}{dt}$, (b) $\frac{dL}{dt}$ and (c) L_{eq} as a function of the viscosity ratio M for different capillary numbers at $u_0 = 0.01$, $\theta = 90^\circ$ and $v_B = 0.48$.

The displacement velocity $\frac{dS}{dt}$ decreases but the change rate of finger length $\frac{dL}{dt}$ increases with increasing capillary number; the displacement velocity is around 0.00667 at the high viscosity ratios and low capillary numbers, which is 2/3 of the maximum inlet velocity u_0; the change rate of finger length is around 0 at high viscosity ratios and low capillary numbers, which means the finger length L tends to an

equilibrium value L_{eq}; and the equilibrium finger length L_{eq} decreases with increasing viscosity ratio or decreasing capillary number.

Effects of surface wettability

Here, the effects of surface wettability are investigated for the contact angles ranging from 20° to 160°. The other parameters are fixed as $M = 1$ with $\upsilon_B = 0.48$ and $Ca = 0.8$. $S(t)$ and $L(t)$ at different times are recorded, and $\frac{dS}{dt}$ and $\frac{dL}{dt}$ can be computed during the displacement. It is found that both $\frac{dS}{dt}$ and $\frac{dL}{dt}$ remain constant during the displacement for each contact angle. The variations of $\frac{dS}{dt}$ and $\frac{dL}{dt}$ with the contact angle are plotted in Figure 9, which follow the linear relations as

$$\frac{dS}{dt}(\theta) = 4.133 \times 10^{-3} - 1.693 \times 10^{-5} \times \theta \tag{48}$$

$$\frac{dL}{dt}(\theta) = 4.946 \times 10^{-3} + 1.583 \times 10^{-5} \times \theta \tag{49}$$

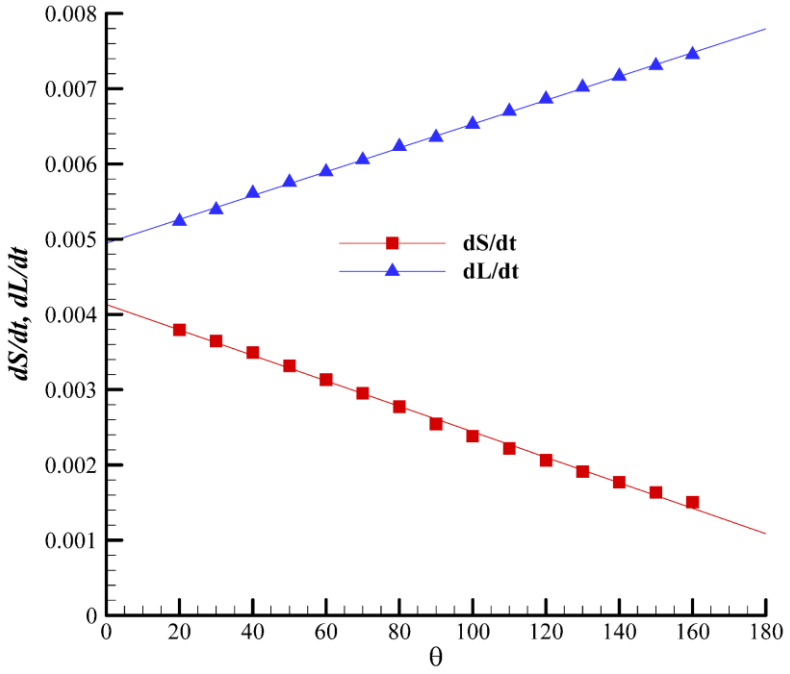

Figure 9. $\frac{dS}{dt}$ and $\frac{dL}{dt}$ as a function of the contact angle θ for $Ca = 0.8$, $M = 1$ and $\upsilon_B = 0.48$. Both $\frac{dS}{dt}$ and $\frac{dL}{dt}$ exhibit a linear dependence on the contact angle with the slope $k = -1.693 \times 10^{-5}$ and 1.583×10^{-5}, respectively.

Conclusion

A new wetting boundary scheme is proposed based on the LB color-gradient model of Liu et al.[4], in which a forcing term proportional to the interface curvature is incorporated to realize the interfacial tension effect. A zero-interfacial-force condition is derived based on the diffuse interface assumption in the contact line region, which is essential for calculation of the interface curvature. We have discussed in details on how the contact angle condition and the zero-interfacial-force condition are properly

implemented in the contact line region. This wetting boundary scheme is first validated by two static problems, i.e. a droplet resting on a flat surface and a cylindrical surface, and one dynamical problem, i.e. the capillary filling in a 2D channel. The present scheme is found to suppress the non-physical mass transfer effectively, and produce smaller spurious velocities. In the static cylindrical surface problem, the present scheme with the eighth-order isotropic discretization for unit normal vector of the solid surface can accurately simulate flows with a broad range of contact angles. In the capillary filling problem, our results agree well with the theoretical solutions for various contact angles and viscosity ratios, and our scheme behaves better than the method proposed by Leclaire et al.[24]. The displacement of immiscible fluids in a 2D channel is then simulated, to study the effect of the surface wettability, capillary number and the viscosity ratio on the displacement process. The displacement velocity and the change rate of finger length both exhibit a linear dependence on the contact angle at the viscosity ratio of unity. The displacement velocity decreases but the change rate of finger length increases with increasing capillary number; the displacement velocity becomes constant at high viscosity ratios and low capillary numbers, which is exactly two-third of the maximum inlet velocity. In contrast to the displacement velocity, the change rate of finger length is around zero for high viscosity ratios and low capillary numbers, which means the finger length tends to an equilibrium value and the equilibrium finger length decreases with increasing viscosity ratio or reducing capillary number. Finally, we interestingly note that the zero-interfacial-force condition can be also derived in the contact line region in 3D. With the zero-interfacial-force condition in contact line region, we have extended the present method to simulation of multiphase flows in 3D geometries, and some convincing results have been obtained, which hopefully will be published in the near future.

Acknowledgments

Y. Yu was supported by the China Scholarship Council for 1 year's study at the University of Strathclyde. H. Liu gratefully acknowledges the financial supports from Thousand Youth Talents Program for Distinguished Young Scholars and the Young Talent Support Plan of Xi'an Jiaotong University.

Funding

This work was supported by the National Natural Science Foundation of China (Nos. 51506168, 51711530130), the National Key Research and Development Project of China (No. 2016YFB0200902), the China Postdoctoral Science Foundation (No. 2016M590943), Guangdong Provincial Key Laboratory of Fire Science and Technology (No. 2010A060801010) and Guangdong Provincial Scientific and Technological Project (No. 2011B090400518).

References

1. Liu H, Kang Q, Leonardi CR, et al. Multiphase lattice Boltzmann simulations for porous media applications. *Computational Geosciences*. 2016; 20: 777-805.
2. Huang H, Sukop MC and Lu X-Y. *Multiphase lattice Boltzmann methods : theory and application*. 2015, p.xiii, 373 pages.
3. Gunstensen AK and Rothman DH. Microscopic Modeling of Immiscible Fluids in Three Dimensions by a Lattice Boltzmann Method. *Europhys Lett*. 1992.

4. Liu H, Ju Y, Wang N, Xi G and Zhang Y. Lattice Boltzmann modeling of contact angle and its hysteresis in two-phase flow with large viscosity difference. *Physical review E, Statistical, nonlinear, and soft matter physics*. 2015; 92: 033306.
5. Shan X and Chen H. Lattice Boltzmann model for simulating flows with multiple phases and components. *Physical Review E*. 1993; 47: 1815-9.
6. Li Q, Luo KH, Kang QJ and Chen Q. Contact angles in the pseudopotential lattice Boltzmann modeling of wetting. *Physical review E, Statistical, nonlinear, and soft matter physics*. 2014; 90: 053301.
7. Huang H, Wang L and Lu X-y. Evaluation of three lattice Boltzmann models for multiphase flows in porous media. *Computers & Mathematics with Applications*. 2011; 61: 3606-17.
8. Gupta A, Sbragaglia M, Belardinelli D and Sugiyama K. Lattice Boltzmann simulations of droplet formation in confined channels with thermocapillary flows. *Physical review E*. 2016; 94: 063302.
9. Swift MR, Orlandini E, Osborn WR and Yeomans JM. Lattice Boltzmann simulations of liquid-gas and binary fluid systems. *Physical Review E*. 1996; 54: 5041-52.
10. Yuan HZ, Chen Z, Shu C, Wang Y, Niu XD and Shu S. A free energy-based surface tension force model for simulation of multiphase flows by level-set method. *Journal of Computational Physics*. 2017; 345: 404-26.
11. Wang Y, Shu C, Huang HB and Teo CJ. Multiphase lattice Boltzmann flux solver for incompressible multiphase flows with large density ratio. *Journal of Computational Physics*. 2015; 280: 404-23.
12. Wang Y, Shu C and Teo CJ. Thermal lattice Boltzmann flux solver and its application for simulation of incompressible thermal flows. *Computers & Fluids*. 2014; 94: 98-111.
13. Wang Y, Shu C and Yang LM. An improved multiphase lattice Boltzmann flux solver for three-dimensional flows with large density ratio and high Reynolds number. *Journal of Computational Physics*. 2015; 302: 41-58.
14. Liu H and Zhang Y. Droplet formation in a T-shaped microfluidic junction. *Journal of Applied Physics*. 2009; 106: 034906.
15. He X and Doolen GD. Thermodynamic Foundations of Kinetic Theory and Lattice Boltzmann Models for Multiphase Flows. *Journal of Statistical Physics*. 2002; 107: 309-28.
16. Yuan H-Z, Niu X-D, Shu S, Li M and Yamaguchi H. A momentum exchange-based immersed boundary-lattice Boltzmann method for simulating a flexible filament in an incompressible flow. *Computers & Mathematics with Applications*. 2014; 67: 1039-56.
17. Yuan H-Z, Shu S, Niu X-D, Li M and Hu Y. A Numerical Study of Jet Propulsion of an Oblate Jellyfish Using a Momentum Exchange-Based Immersed Boundary-Lattice Boltzmann Method. *Advances in Applied Mathematics and Mechanics*. 2015; 6: 307-26.
18. Tian FB, Dai H, Luo H, Doyle JF and Rousseau B. Fluid-structure interaction involving large deformations: 3D simulations and applications to biological systems. *J Comput Phys*. 2014; 258.
19. Tian FB, Luo H, Zhu L, Liao JC and Lu XY. An efficient immersed boundary-lattice Boltzmann method for the hydrodynamic interaction of elastic filaments. *J Comput Phys*. 2011; 230: 7266-83.
20. Huang H and Lu X-Y. An ellipsoidal particle in tube Poiseuille flow. *Journal of Fluid Mechanics*. 2017; 822: 664-88.
21. Sbragaglia M and Succi S. Analytical calculation of slip flow in lattice Boltzmann models with kinetic boundary conditions. *Physics of Fluids*. 2005; 17: 093602.
22. Huang H, Thorne DT, Jr., Schaap MG and Sukop MC. Proposed approximation for contact angles in Shan-and-Chen-type multicomponent multiphase lattice Boltzmann models. *Physical review E, Statistical, nonlinear, and soft matter physics*. 2007; 76: 066701.
23. Latva-Kokko M and Rothman DH. Static contact angle in lattice Boltzmann models of immiscible fluids. *Physical review E, Statistical, nonlinear, and soft matter physics*. 2005; 72: 046701.

24. Leclaire S, Abahri K, Belarbi R and Bennacer R. Modeling of static contact angles with curved boundaries using a multiphase lattice Boltzmann method with variable density and viscosity ratios. *International Journal for Numerical Methods in Fluids*. 2016; 82: 451-70.
25. Chen HY, Jasnow D and Vinals J. Interface and contact line motion in a two phase fluid under shear flow. *Physical review letters*. 2000; 85: 1686-9.
26. Ding H and Spelt PD. Wetting condition in diffuse interface simulations of contact line motion. *Physical review E, Statistical, nonlinear, and soft matter physics*. 2007; 75: 046708.
27. Jacqmin D. Contact-line dynamics of a diffuse fluid interface. *Journal of Fluid Mechanics*. 2000; 402: 57-88.
28. Sui Y, Ding H and Spelt PDM. Numerical Simulations of Flows with Moving Contact Lines. *Annual Review of Fluid Mechanics*. 2014; 46: 97-119.
29. Jacqmin D. Calculation of two-phase Navier-Stokes flows using phase-field modeling. *Journal of Computational Physics*. 1999; 155: 96-127.
30. Ye T, Shyy W and Chung JN. A Fixed-Grid, Sharp-Interface Method for Bubble Dynamics and Phase Change. *Journal of Computational Physics*. 2001; 174: 781-815.
31. Briant AJ, Papatzacos P and Yeomans JM. Lattice Boltzmann simulations of contact line motion in a liquid-gas system. *Philosophical transactions Series A, Mathematical, physical, and engineering sciences*. 2002; 360: 485-95.
32. Khatavkar VV, Anderson PD and Meijer HEH. Capillary spreading of a droplet in the partially wetting regime using a diffuse-interface model. *Journal of Fluid Mechanics*. 2007; 572: 367.
33. Qian T, Wang X-P and Sheng P. A variational approach to moving contact line hydrodynamics. *Journal of Fluid Mechanics*. 2006; 564: 333.
34. Liu H, Valocchi AJ and Kang Q. Three-dimensional lattice Boltzmann model for immiscible two-phase flow simulations. *Physical review E, Statistical, nonlinear, and soft matter physics*. 2012; 85: 046309.
35. Liu H, Valocchi AJ, Werth C, Kang Q and Oostrom M. Pore-scale simulation of liquid CO2 displacement of water using a two-phase lattice Boltzmann model. *Advances in Water Resources*. 2014; 73: 144-58.
36. Lishchuk SV, Care CM and Halliday I. Lattice Boltzmann algorithm for surface tension with greatly reduced microcurrents. *Physical review E, Statistical, nonlinear, and soft matter physics*. 2003; 67: 036701.
37. Halliday I, Law R, Care CM and Hollis A. Improved simulation of drop dynamics in a shear flow at low Reynolds and capillary number. *Physical review E, Statistical, nonlinear, and soft matter physics*. 2006; 73: 056708.
38. Halliday I, Hollis AP and Care CM. Lattice Boltzmann algorithm for continuum multicomponent flow. *Physical review E, Statistical, nonlinear, and soft matter physics*. 2007; 76: 026708.
39. Lallemand P and Luo LS. Theory of the lattice boltzmann method: dispersion, dissipation, isotropy, galilean invariance, and stability. *Physical review E, Statistical physics, plasmas, fluids, and related interdisciplinary topics*. 2000; 61: 6546-62.
40. Guo Z, Zheng C and Shi B. Discrete lattice effects on the forcing term in the lattice Boltzmann method. *Physical review E, Statistical, nonlinear, and soft matter physics*. 2002; 65: 046308.
41. Brackbill JU, Kothe DB and Zemach C. A continuum method for modeling surface tension. *Journal of Computational Physics*. 1992; 100: 335-54.
42. Xu Z, Liu H and Valocchi AJ. Lattice Boltzmann simulation of immiscible two-phase flow with capillary valve effect in porous media. *Water Resources Research*. 2017; 53: 3770-90.
43. Sbragaglia M, Benzi R, Biferale L, Succi S, Sugiyama K and Toschi F. Generalized lattice Boltzmann method with multirange pseudopotential. *Physical review E, Statistical, nonlinear, and soft matter physics*. 2007; 75: 026702.

44. Kang Q, Zhang D and Chen S. Displacement of a two-dimensional immiscible droplet in a channel. *Physics of Fluids*. 2002; 14: 3203-14.
45. Huang H, Huang JJ and Lu XY. Study of immiscible displacements in porous media using a color-gradient-based multiphase lattice Boltzmann method. *Computers & Fluids*. 2014; 93: 164-72.
46. Diotallevi F, Biferale L, Chibbaro S, et al. Capillary filling using lattice Boltzmann equations: The case of multi-phase flows. *The European Physical Journal Special Topics*. 2009; 166: 111-6.
47. Chin J, Boek ES and Coveney PV. Lattice Boltzmann simulation of the flow of binary immiscible fluids with different viscosities using the Shan-Chen microscopic interaction model. *Philosophical transactions Series A, Mathematical, physical, and engineering sciences*. 2002; 360: 547-58.
48. Kang Q, Zhang D and Chen S. Immiscible displacement in a channel: simulations of fingering in two dimensions. *Advances in Water Resources*. 2004; 27: 13-22.
49. Dong B, Yan YY, Li W and Song Y. Lattice Boltzmann simulation of viscous fingering phenomenon of immiscible fluids displacement in a channel. *Computers & Fluids*. 2010; 39: 768-79.
50. Shi Y and Tang GH. Simulation of Newtonian and non-Newtonian rheology behavior of viscous fingering in channels by the lattice Boltzmann method. *Computers & Mathematics with Applications*. 2014; 68: 1279-91.
51. Zou Q and He X. On pressure and velocity boundary conditions for the lattice Boltzmann BGK model. *Physics of Fluids*. 1997; 9: 1591-8.